

# Stellar Karaoke: Deep Blind Separation of Terrestrial Atmospheric Effects out of Stellar Spectra by Velocity Whitening

Nima Sedaghat<sup>1</sup>, J. Bryce Kalmbach<sup>1</sup>, Brianna M. Smart<sup>1</sup>, and Erin L. Howard<sup>1</sup>

DIRAC Institute and the Department of Astronomy, University of Washington, 3910 15th Avenue NE, Seattle, WA 98195, USA  
e-mail: nimaseda@uw.edu

2022-12-31

## ABSTRACT

We exploit the statistical independence of stellar features and atmospheric adversarial effects in stellar spectra, to remove the latter from observed signals using a fully unsupervised data-driven approach. Concretely, we first increase the inter-observation entropy of telluric absorption lines by imposing a random, virtual radial velocity to the observed spectrum. This novel “trick” results in a non-standard form of “whitening” in the atmospheric components of the spectrum, decorrelating them across multiple observations. Then we use deep convolutional auto-encoders, to learn a feature-space in which the two “sources” of information, stellar and atmospheric, are easily separable, leading to removal of the latter. We apply the process on spectra from two different data collections: ~250,000 HARPS spectra and ~660,000 from SDSS.

We compare and analyze the results across datasets, as well as with existing tools, and discuss directions for utilizing the introduced method as a fast and more reliable tool in the future.

**Key words.** stellar spectra – telluric lines – deep learning – unsupervised – whitening – decorrelation – source separation

arXiv:2301.00313v1 [astro-ph.SR] 1 Jan 2023

## 1. Introduction

Throughout this paper, we introduce and elaborate a method based on signal processing tricks combined with a fully unsupervised deep neural network to remove the non-linear, time-variant effect of telluric lines out of observed spectra without any need for manual modeling and tuning. Concretely, we show how looking at an enormous dataset of spectra reveals new insights into their features, allowing for novel solutions to existing, difficult problems.

In ground-based observations of stellar spectra, it is not unusual for the source’s spectrum to reach our detectors in an altered state. The spectrum may be affected by a number of events in space (redshift/blueshift, emission, absorption, etc.). When finally reaching the Earth, the photons in the spectrum will undergo additional transformations as they travel through the Earth’s atmosphere and are collected by telescopes. Telescope effects are often well characterized and constrained (CCD noise, fringing, mirror defects, etc.). However, other effects are usually more difficult to model and correct.

Particularly, passing through the terrestrial molecules present in the Earth’s atmosphere results in absorption lines in the sensed spectrum. These absorption lines, known as telluric lines, are the results of interaction of photons with molecules due to a number of electron, rotational, and vibrational transitions, and are a persistent source of contamination and loss of information in the observed spectra. The majority of the molecules responsible for absorption are O<sub>2</sub>, H<sub>2</sub>O, CO<sub>2</sub>, CH<sub>4</sub>, O<sub>3</sub>, N<sub>2</sub>O, and the Chappuis ozone absorption bands. The many of these absorption features lie in the near-infrared and ultraviolet part of the electromagnetic spectrum, with weaker absorption features from ozone, oxygen, and water present in optical wavelengths. Additional emission features are also added to the spectrum as photons are emitted from the molecules. The emission features are relatively straight-

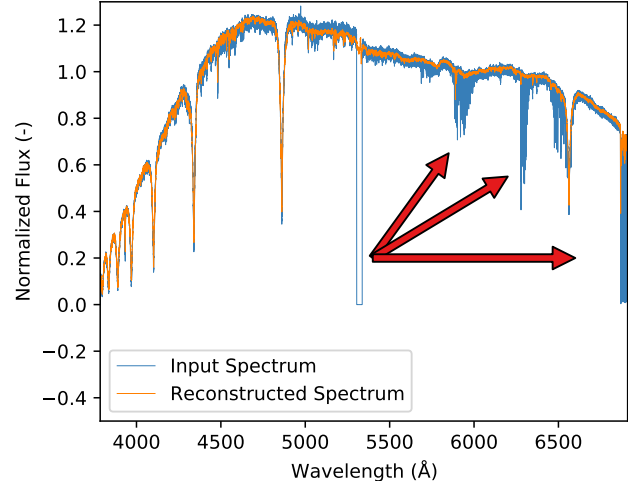


**Fig. 1.** We exploit the statistical properties of stellar spectra in large datasets, pass them through a convolutional auto-encoder, and get telluric lines rejected with close to zero effort.

forward to handle by observing source-free portions of the sky. Observed emission lines in “empty” regions provide an easily accessible template for emission removal. The absorption features are more complicated, scaling non-linearly, and are affected by atmospheric conditions at the time of observation.

Most of the traditional methods used for the removal of telluric lines consider each spectrum as a single independent entity, discarding the set of observed spectra as a whole – e.g. see Hrudková & Harmanec (2005). One group of such methods use standard stars to assist with atmospheric line removal. They do

this by observing standard stars with relatively featureless spectra and using them as atmospheric templates. This is often done by observing A0V or G-type stars, though this is predominantly used at the near-infrared and IR wavelengths (Vacca et al. 2003; Artigau et al. 2014). The reference star should be ideally located near the target star and observed close in time to measure the atmospheric conditions as accurately as possible. The target source's spectrum is then divided by the telluric template. However, this method is limited if there are no such standard stars available during an observing run or if observing conditions result in a poor spectrum. Atmospheric absorption can also vary rapidly, on the order of minutes, requiring significant time and resources dedicated to observing the template stars. The division is an iterative process requiring wavelength and intensity scaling adjustments to match the atmospheric effects.

Another common method is to model the Earth's atmosphere and create a synthetic spectrum which precisely models the atmospheric absorption. These models solve the radiative transfer equation of the Earth's atmosphere using numerical models – e.g. Allart et al. (2022). These methods are dependent on atmospheric conditions measurements from the night's observations. This is commonly done with programs such as `molecfit` (Smette et al. 2015) and `telfit` (Gullikson et al. 2014). The radiative transfer code retrieves the temperature, pressure, and humidity from the time of observation and uses a database of molecular parameters to create a fit for the telluric absorption. While this technique is relatively successful, it may perform poorly if there are a large number of intrinsic features, little or no continuum, low signal-to-noise ratio (S/N), or large airmass observations with high water vapor content. Moreover, current implementations of this technique suffer from rather slow performance to the extent that fitting a model to a single spectrum may take up to several minutes on today's computers. See Ulmer-Moll et al. (2019) for a comparison of the above methods.

More recent methods, however, have incorporated implicit modeling of the spectra by looking at a set of examples, potentially eliminating the need for manual, explicit modeling. Such methods, loosely dubbed data-driven approaches, have gained good momentum in the past couple of decades. Particularly in astronomy, a data-driven look at spectra has been mainly incorporated in the broad context of dimensionality reduction.

Arguably the most popular dimensionality reduction method used in astronomy has been the Principal Component Analysis (PCA – see Jolliffe & Cadima (2016) for a review), which has been used as a dimensionality reduction tool on astronomical spectra for many years now. Connolly et al. (1995) used it to classify galaxy spectra with only the first two principal components while Bailer-Jones et al. (1998) showed that PCA can compress stellar spectra by a factor of over 30 and classify anomalous and non-stellar spectra in the data set. Furthermore, Bailer-Jones et al. (1998) found that the compression removed noise as well as bogus features in the spectra such as dust appearing on the plate during plate scanning. Some works such as Artigau et al. (2014), even attempt to remove telluric lines of a few specific objects in the HARPS dataset using PCA decomposition and demonstrate improved radial velocity measurement accuracy. However, their method does not operate solely on the stellar spectra and still requires observations of telluric standard stars. Our approach solely requires a set of input stellar spectra without specific telluric standard stars.

Moreover, the very important, but often overlooked point about applicability of PCA for such applications, is its linear nature, making it unable to account for modeling non-linear phenomena by definition. E.g. in the case of telluric lines, a method

simply based on PCA, may not be able to tell the difference between a telluric and stellar line, in crowded regions of the wavelength. This inability has been well observed as early as in Bailer-Jones et al. (1998). In this work, we show how transformation to a more sophisticated feature space is necessary for such a task.

There is a closely related family of neural networks known as encoder-decoder networks (fig. 2). The *contraction* part compresses the input to an often low-dimensional representation, also known as "latent representation" or simply "code". The *expansion* part is then used to *decode* this low-dimensional representation up to the desired output. The transformation used for coding (and decoding) is learned during training, according to the task at hand. A special case of such networks, *auto-encoders*, is an unsupervised network trained to reconstruct the input without the need for labeled input data. As described in Hinton & Salakhutdinov (2006) these networks can be used to reduce the dimensionality of input data in a non-linear generalization of PCA.

In Yang & Li (2015) the authors use a classical (non-convolutional) auto-encoder to transform 3000-dimensional spectra from the Sloan Digital Sky Survey (SDSS) Data Release 7 (Abazajian et al. 2009) to lower-dimensional features, which are later used for estimation of atmospheric parameters. Wang et al. (2016a) also used classical (non-convolutional) auto-encoders for feature learning on astronomical spectra. They compare spectral classification based on their learned features with PCA and locally linear embedding (LLE), an alternate non-linear dimensionality reduction method. They find that their auto-encoder approach performs the best when classifying spectra among a data set of F, G and K-type stars.

One problem with the mere use of auto-encoders, especially for applications in (astro-)physics, is the entangled mapping of concepts into the reduced signal – the latent space. The Variational AutoEncoder (VAE: Kingma & Welling 2014) has shown to mitigate this effect to some extent. Portillo et al. (2020) used a VAE to reconstruct SDSS galaxy spectra resampled to an input spectrum with 1000 components. They found that when limiting the dimensionality of the latent spaces to 2, 4, 6 or 10 components ( $\geq 99\%$  compression) the VAEs and traditional autoencoders both reconstructed SDSS galaxy spectra with a lower reconstruction error than PCA and non-negative matrix factorization (NMF) applied with the same number of components. The authors then demonstrated that different galaxy classes occupied different areas of the latent space enabling classification.

Classical auto-encoders are merely composed of fully-connected layers and thus suffer from a lack of scalability to deeper networks and high-dimensional data – usually the case in modern astronomical spectroscopy. We address this drawback by incorporating convolutional (and up-convolutional) layers for transformation of data to the desired feature space; an idea borrowed from computer vision. In Zhang et al. (2004) the authors map images of people's faces to low-dimensional manifolds, and reconstruct them back. They find a correlation between the face pose and the low-dimensional manifold, independently of the person in the image. Wang et al. (2016b) shows comprehensive experiments on dimensionality reduction using auto-encoders, and studies the effects of different latent dimensions using synthetic and real images. Note that in case of spectra, the networks need to be updated to use 1D (up-)convolutional layers, as opposed to 2D in case of images.

Perhaps the closest to our work, both in terms of the used network architecture, as well as the data-driven unsupervised concept is Sedaghat et al. (2021), where a convolutional VAE

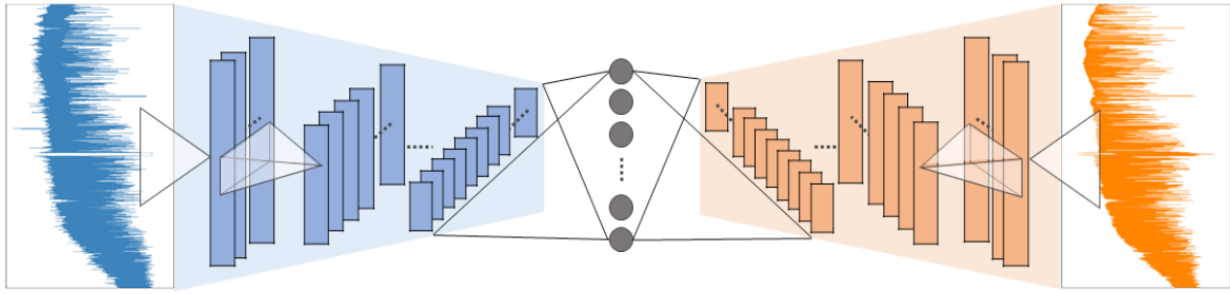


**Fig. 2.** A simple auto-encoder trained to reconstruct stellar spectra, can decompose physically meaningful components out of the input, when the compression is high enough and the number of convolutional kernels is limited. Blue is the input spectrum and orange is the reconstructed version. The region annotated by the red circle indicates a high density of such reconstruction rejections.

is used to extract knowledge from a large number of HARPS spectra, in a fully unsupervised manner. We borrow and use the exact same neural architecture for our work. However, we additionally utilize the conceptual decomposition of stellar features and atmospheric effects into two different spectra; an idea that turns out to have been touched as early as in Hadzrava (1997), however without a data-driven perspective.

## Our Contributions

- We process a huge number of very high-dimensional spectra as a whole, letting statistical properties emerge in them, allowing to be treated as random processes.
- We model the telluric components in stellar spectra as independent stars and impose a virtual radial velocity on them to achieve statistical whitening/decorrelation.
- We incorporate a convolutional auto-encoder, that automatically acts as a source separation tool, rejecting telluric lines in a fully unsupervised fashion, with zero explicit modeling.

## 2. Problem Formulation

We seek to clean adversarial atmospheric effects out of an arbitrary observed signal,  $x$ . The observed signal in our case is a stellar spectrum, and so is a function of wavelength,  $\lambda$ , letting us denote it as  $x(\lambda)$ .

We use the below formulation to model the various phenomena affecting a stellar spectrum, before it is captured by our sensors:

$$x(\lambda) = (s(\lambda) \times t(\lambda)) * h(\lambda) + n(\lambda) \quad (1)$$

where  $s$  is the stellar spectrum, incorporating line-of-sight effects from relative stellar velocity and the interstellar medium.  $t$  is an imaginary signal representing the telluric lines affecting the spectrum.  $x$  is the observed signal: a single spectrum that takes on different values at each wavelength depending on the flux at that wavelength. So we use the notation,  $x(\lambda)$ , throughout this article.

We use  $h$  to denote what we call the observation transfer function, and models the changes the signal goes through during the sensing process, and includes, but is not limited to, the

line spread function, etc.  $n$  models the additive noise which is not modeled in the transfer function,  $h$ .

We work with a large ensemble of  $N$  observations, mostly coming from different sources. We use the subscript,  $i$ , to differentiate between various observations:

$$x_i(\lambda) = (s_i(\lambda) \times t_i(\lambda)) * h(\lambda) + n_i(\lambda) \quad i \in \{1, 2, \dots, N\} \quad (2)$$

Note that the spectrum,  $s$ , depends on  $i$ , as we work with various objects at the same time. The atmospheric conditions are also time-variant, an important point that is reflected in dependence of  $t$  on  $i$ . The same is true for noise,  $n$ . Without loss of generality, and for the sake of simplicity, we assume that  $h$  is constant across the whole set of observations.

We seek to eliminate the effect of telluric lines from the observed signal, which in this model is equal to extracting  $s_i(\lambda) * h(\lambda)$  for every observation – note that removal of the *observation effect*,  $h$ , is not part of the objective here.

We also model the effect of the radial velocity,  $v$ , of the target object on the observed spectrum,  $s$  as:

$$s_i(\lambda) = \mathcal{V}\{\dot{s}_i(\lambda), v_i\} = \dot{s}_i\left(\lambda\left(1 - \frac{v_i}{c}\right)\right) \quad (3)$$

where  $\dot{s}_i$  would be the observed spectrum, if the radial velocity was zero – i.e. no Doppler shift. We call  $\dot{s}_i$  the *static spectrum* hereafter. The  $\mathcal{V}\{\cdot\}$  operator represents the effect of the radial velocity,  $v_i$ , on the spectrum, as expanded in the second line of the above equation, and  $c$  is the speed of light. The physical units of  $v_i$  and  $c$  can be arbitrarily chosen, as long as they are kept the same.

$t_i$  on the other hand, and by definition, do not have any dependence on  $v_i$ , and therefore can be modeled as:

$$t_i(\lambda) = \mathcal{V}\{\dot{t}_i(\lambda), 0\} \quad (4)$$

### 2.1. Continuous vs. Discrete

All the signals discussed above are of continuous nature up until the point they are sensed by the detector. Sensing by the detector

is a process that involves sampling as one of its steps, converting a spectrum into a series of real-valued samples. Therefore, the data we work with in our experiments is the discrete representation of  $x_i(\lambda)$ , namely  $X_i^l$  – we use  $l$  as the discrete-valued index for the sampled pixels.

However, for the reasons below, keeping the formulation in the continuous representation is safe – and clearer. First, the signals modeled so far are all the constituent elements of the pre-sampling signal,  $x_i(\lambda)$ , and so the continuous models hold. Secondly, the only part of our method which explicitly modifies the signal along the wavelength axis, the  $\mathcal{V}\{\cdot\}$  operator (section 3.1), does its job by regressing the interpolated version of the signal; practically converting the discrete signal back to its continuous version, applying the transformation and sampling it back again to the discrete space. Therefore mathematical definition of the operator in the continuous space is valid.

## 2.2. Signals as Random Processes

The process of sensing a signal,  $x_i$ , from an arbitrarily chosen object in the sky, which is affected by many non-deterministic phenomena along the way, can be seen as one realization of a random process. In other words, the set of  $x_i$ , or their discrete representation,  $X_i$ , for various  $i$ , represent an ensemble of realizations of a random process,  $\{X\}$ <sup>1</sup>. Note that in this particular application, the index set of the random process is sampled from wavelengths,  $\lambda$  – a bit counter-intuitive, as it is usually of a temporal nature in typical applications.

Therefore each  $X^l$  represents a random variable, with outcomes  $X_i^l$ . Similarly, we can model  $\{S\}$ ,  $\{\dot{S}\}$  and  $\{T\}$  as discrete-index random processes of the same type.  $\{S\}$  is then a generator of various *clean* spectra,  $S_i$ , while  $\{\dot{S}\}$  generates the static  $\dot{S}_i^l$  spectra. As we will see in the next section, this non-deterministic view on signals allows us to explain the statistical operations and properties of the components more clearly.

## 3. Method

The method is composed of two key steps:

- Increasing the entropy of telluric components across observations and,
- transforming the spectra into a space where the stellar and telluric components are separable, then removing the non-dominant one.

**Median Normalization** As a pre-processing step, we normalize each spectrum in the dataset based on its *median*, to mitigate the effect of different distances in sources, which otherwise results in extreme inter-sample flux range variations.

### 3.1. Velocity Whitenning

In the default conditions, the spectroscopic observations are in the so-called topocentric reference frame where the telluric lines, if they exist, take on the same wavelengths – or pixels locations. What it means from a statistical point of view though is this:

Let us assume, for simplicity, that all the observed objects have the same static spectra,  $\dot{S}_i(\lambda)$ . The resulting spectra,  $s_i(\lambda)$

would then only be different based on their radial velocities,  $v_i$ , which, by definition, are modeled as scaling transformations along the wavelength axis (eq. (3)). Note that since  $v_i$  are outcomes of a random variable,  $s_i(\lambda)$  are consequently still highly independent and uncorrelated.

$t_i$  on the other hand, are composed of a set of absorption lines with different strengths, but all happening at pre-defined specific wavelengths. This feature makes them highly correlated across multiple observations and easy to fit for any model – fig. 3, left column.

To decrease the existing correlation between realizations of the telluric signals, we increase the entropy across  $t_i$  by randomizing them using an emulated radial velocity,

$$t'_i(\lambda) = \mathcal{V}\{\dot{t}_i(\lambda), v'_i\} \quad (5)$$

where each  $v'_i$  is a random velocity and is drawn from  $V' : \mathbb{R} \rightarrow \mathbb{R}$ . The above effect can be implemented by simply contracting or expanding the wavelength axis, according to eq. (3). Note though that this is a purely artificial phenomenon, and although it is chosen to have the same effect as the “real” radial velocity of stars, it has no particular meaning for telluric lines<sup>2</sup>.

In practice, however, we only have access to the observed signal,  $x$ , and not its forming components. Hence the proposed randomization cannot be applied directly on  $t$  alone, and the whole observed signal gets affected. But in the below, we show that it can still have the desired effect:

$$\lambda \rightarrow \lambda'_i = \lambda \times \left(1 - \frac{v'_i}{c}\right) \quad (6)$$

$$\begin{aligned} x'_i(\lambda) &= \mathcal{V}\{x_i(\lambda), v'_i\} \\ &= \mathcal{V}\{(s_i(\lambda) \times t_i(\lambda)) * h(\lambda) + n_i(\lambda), v'_i\} \\ &= \mathcal{V}\{(s_i(\lambda) \times t_i(\lambda)) * h(\lambda), v'_i\} + \mathcal{V}\{n_i(\lambda), v'_i\} \end{aligned} \quad (7)$$

which, according to the proof provided in appendix A becomes:

$$\begin{aligned} x'_i(\lambda) &= \left(1 - \frac{v'_i}{c}\right) \mathcal{V}\{s_i(\lambda) \times t_i(\lambda), v'_i\} * \mathcal{V}\{h(\lambda), v'_i\} + \mathcal{V}\{n_i(\lambda), v'_i\} \\ &= \left(1 - \frac{v'_i}{c}\right) (s_i(\lambda'_i) \times t_i(\lambda'_i)) * h(\lambda'_i) + n_i(\lambda'_i) \end{aligned} \quad (8)$$

Now since  $\left(1 - \frac{v'_i}{c}\right)$  is, for each  $x'_i$ , a constant coefficient and is normalized out before being passed to the next step of the method, we can see that the emulated randomized velocity has found its way from  $x_i$  down to  $t_i$ . In other words, we have achieved the required velocity randomization in  $t_i$  by modifying  $x_i$ . The two main components in the *tweaked* signal can now be rewritten as:

$$\begin{aligned} \text{Telluric:} & \quad \text{Stellar:} \\ \mathcal{V}\{\dot{t}_i(\lambda), v'_i\} & \quad \mathcal{V}\{\dot{s}_i(\lambda), v_i + v'_i\} \end{aligned}$$

So, we have achieved two components which are virtually moving independently of each other, when going over various observations. Figure 3 illustrates this effect in practice.

<sup>1</sup> The term *random* in this context is not in contradiction with the *structure* in stellar spectra. The structure is encoded in the basic parameters of the constituent set of random variables, such as the expected value and covariance matrix.

<sup>2</sup> A similar deterministic effect occurs when taking stellar spectra to the barycentric frame.

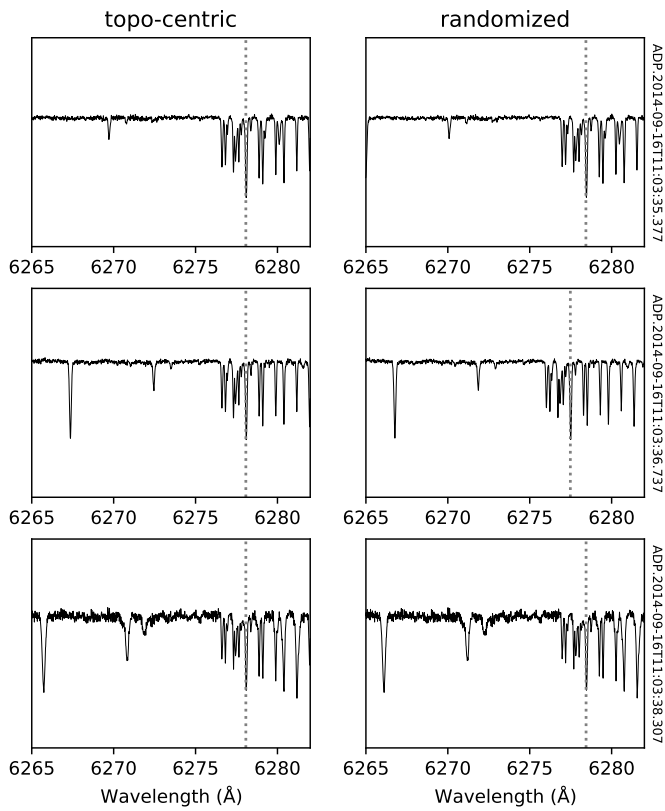


**Fig. 3.** On the left a set of exemplar spectra are depicted. Stellar lines are unaligned due to different radial velocities. But telluric lines are aligned, even though they may have different shapes due to their inherent time dependence (the dotted vertical line indicates the location of a specific telluric line in all plots). On the right the same spectra after velocity randomization are depicted. Telluric lines are now unaligned too, but with a pattern different to that of stellar lines!

From a statistical point of view, what we achieve with the above velocity randomization is a degree of “whitening” of the telluric random process,  $\{T\}$ . More precisely, we decrease the mutual correlation between every pair,  $(T^l, T^m)$ , pushing the statistical behavior of the telluric component toward white noise (Li & Zhang 1998; Eldar & Oppenheim 2003; Kessy et al. 2018). Note again that  $(T^l, T^m)$ , the random variables we try to decorrelate, are each defined on a single pixel of the spectrum, and their outcomes vary along with different observations. A visualization of the results of the above whitening process is illustrated in section 5.

### 3.2. Deep Feature Space

We borrow and use the exact architecture of the 1D convolutional auto-encoder introduced by Sedaghat et al. (2021) – Figure 2. The convolutional layers of the *encoder* transform the input spectrum down to a pre-defined number of “latent variables” at the bottleneck of the network. This low-dimensional representation of the input, also known as the “code”, is the most compressed version of the input spectrum. The dimensionality of this vector is chosen based on the desired compression rate in various experiments. Note though that in the VAE version of our networks, which is the case in most of the experiments of this work, the latent nodes are implemented probabilistically, each being modeled with a pair of scalars: mean and std of a normal distribution. On the other side of the bottleneck, the decoder re-

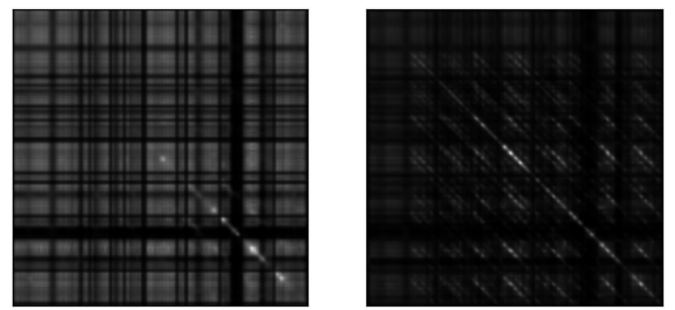


**Fig. 4.** Visual illustration of the covariance matrix of the ensemble of signals, before and after whitening. On the left, the covariance matrix of the  $[6275, 6285]\text{\AA}$  region for some subset of size 90 of the observations is visualized. On the right, the same is done *after* velocity whitening, where  $v_i$  were sampled from the uniform distribution:  $V \sim U(-30\text{km/s}, 30\text{km/s})$ . The covariance matrix is closer to the identity matrix now, confirming achievement of some degree of whitening/decorrelation.

ceives the compressed code and takes it step-by-step up to the same dimension as the original input ( $2^{18} + 2^{16}$  for HARPS). We keep using the same per-pixel L1 end-to-end loss function, as introduced in the original work, to achieve acceptable pixel-level accuracy.

This ~typical architecture has proven to be able to transform the input to a space where noise-like components of the signal are easily separable. As we show with our experiments, the statistical trick developed in the previous section pushes the telluric components farther from the stellar features and closer to the noise, in the learned feature space, letting them be rejected as easily as noise.

We of course need to constrain the reconstruction abilities of the network with a high compression rate as well as a variational loss at the bottleneck, not to have too strong of a network capable of fitting the two independent components at the same time!

## 4. Data

We use data from two publicly available collections: HARPS and SDSS. Our main experiments are run on HARPS, while SDSS is used as a difficult test-bench.

### 4.1. HARPS

HARPS (High Accuracy Radial-velocity Planet Searcher; Mayor et al. 2003) is an instrument on the 3.6m La Silla Telescope. It is a fibre-fed high-resolution echelle spectrograph dedicated to the discovery of exoplanets, with a spectral resolution of  $R = 115,000$  and covers the spectral range  $378\text{--}691\text{nm}$ <sup>3</sup>. The data used has been instrument-corrected and detector-corrected, as well as sky-subtracted.

Our downloaded dataset initially consisted of 272376 total spectra, which after automatic removal of corrupted files, NaNs and noise-like ones, was reduced to 267361 “stable” ones. This collection is mainly composed of stellar spectra. However, there are some random contaminant objects too, such as SUN, MOON, etc., which we allowed to enter our training set on purpose, to increase robustness of the learned features. We trimmed, regridded and homogenized all spectra before being passed to the

<sup>3</sup> [http://archive.eso.org/wdb/wdb/adp/phase3\\_main/form](http://archive.eso.org/wdb/wdb/adp/phase3_main/form)

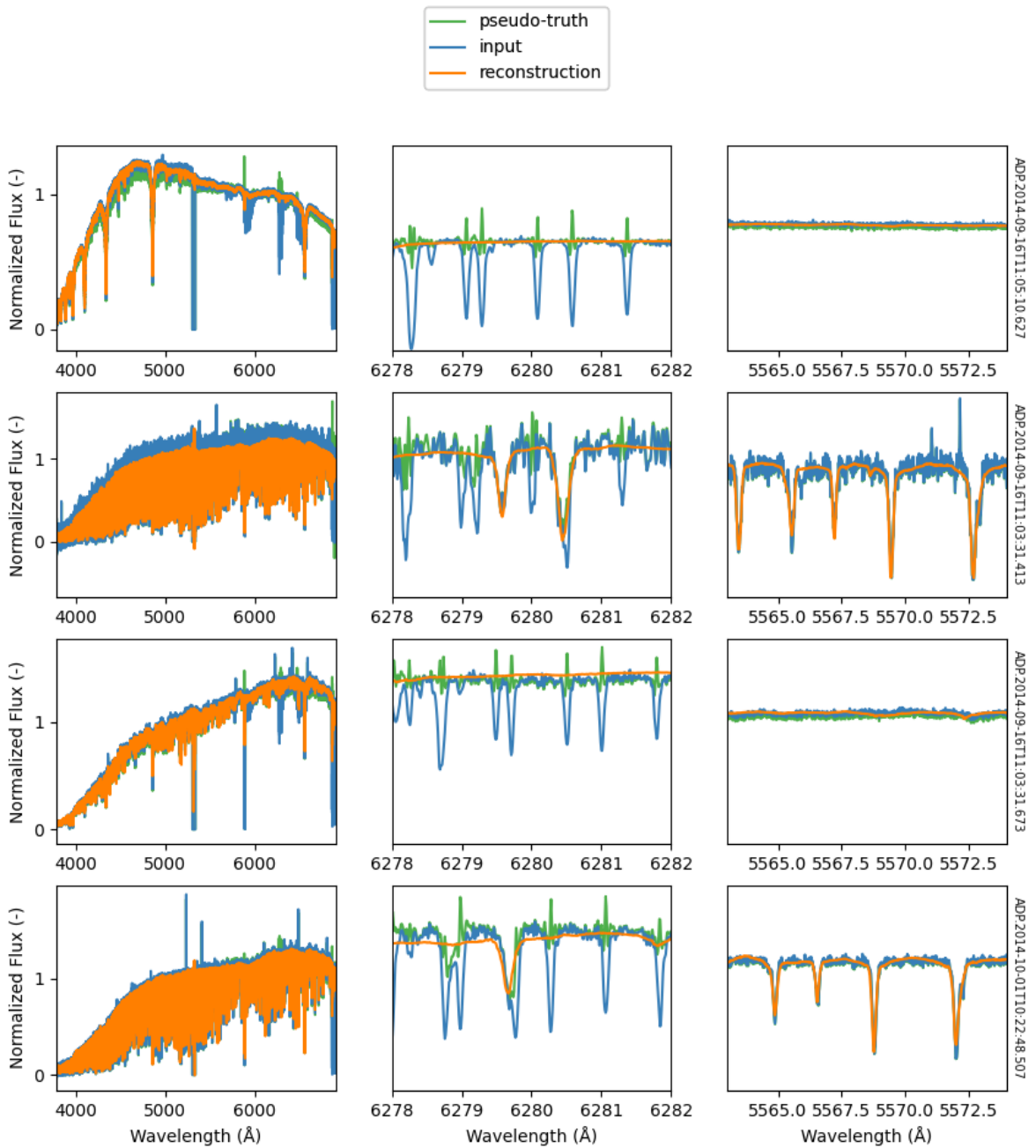


**Fig. 5.** Results Qualitative illustration of the results on an exemplar selection of HARPS spectra. Each row depicts one spectrum, with its HARPS ID written on the right, while columns focus on different regions of interest. Interpretation hint: reconstruction (orange) should follow the pseudo-truth (molecfit: green). The left-most column covers the whole spectrum, as is fed into the network, and illustrates the robustness of the network to different characteristics of the spectra (continuum, noise level, etc.). Major stellar lines such as  $H\alpha$  can be easily spotted in the less ‘busy’ examples. In the middle column we zoom in on a potentially complex region where narrow stellar lines, when existing, can collide with telluric lines of similar shapes. E.g. in the second and 4th row there are examples of such cases, where the network rejects the telluric component, while still preserving the stellar part very well – thus rejecting the hypothesis that it might be simply rejecting narrow lines by applying a moving average. In the third column, we focus on a region where similarly narrow stellar lines occur in some of the spectra, but not in the others. This way we reject the hypothesis that the network might have ‘memorized’ the locations of the lines. Note that the network (orange) is even outperforming the pseudo-truth (green) in some cases, illustrating a smoother, more robust reconstruction in abrupt changes.

network in exactly the same way as is done by Sedaghat et al. (2021).

Note that the pipeline the HARPS spectra go through is set up such that the spectra are automatically transformed to the

barycentric reference frame and re-gridded before being stored in the archive. The originally captured version, in the topocentric reference frame, is also not preserved. Therefore we had to transform them back to the topocentric frame for our experiments.

ments. Although this is touching the core concept of our presented method, it turned out to be a safe procedure: transformation to the barycentric frame exerts added randomness on the radial velocity, which is perfectly compatible with our method. In fact, our method has been inspired by observing traces of the above-mentioned fact in our initial experiments.

## 4.2. SDSS

Our second dataset consisted of spectra from the SEGUE (Yanny et al. 2009) and SEGUE-2 spectroscopic surveys (Rockosi et al. 2022) that were part of the larger Sloan Digital Sky Survey (SDSS). The SEGUE surveys both used the 2.5m Sloan Foundation Telescope (Gunn et al. 2006) located at Apache Point Observatory with the two original Sloan Digital Sky Survey fiber spectrographs (Smee et al. 2013). The SDSS spectrographs have a resolution of  $R \sim 1800$  and together have 640 fibers (320 each) that plug into aluminum "plugplates" for each observation. In each plate 32 plugs are reserved for blank sky observations and 16 for spectrophotometric standard stars in the field. Each spectrograph has a red and a blue channel that collect data on separate CCDs with the blue wavelength range from approximately 3800 Å to 6100 Å and the red wavelengths spanning approximately 5900 Å to 9200 Å. Sources in the original SEGUE survey sampled Milky Way stars at a variety of distances, colors and metallicities while the SEGUE-2 targets focused on stars in the Milky Way halo.

In our experiments we used the ~660,000 uncalibrated spectra from the red CCD of one of the spectrographs (labeled as 'r1' in the SDSS data archive) provided with SDSS Data Release 17 (Abdurro'uf et al. 2022) and accessible via the DR17 FITS website<sup>4</sup>. The uncalibrated spectra consist of multiple 10-30 minute exposures of each source. Since the SEGUE surveys imaged each source multiple times to create coadded spectra this means we have multiple spectra in our dataset for the same source. For each plate we exclude the fibers that were intentionally pointed at empty patches of sky and labelled "SKY" in the data.

The uncalibrated spectra used are labelled 'spFrame' in the SDSS data model<sup>5</sup> and according to the details of the SDSS spectroscopic pipeline (Stoughton et al. 2002) they are flat-fielded but not flux-calibrated. The flux calibration spectra ('spFluxCalib' in the data model) include telluric absorption calculated by the spectroscopic pipeline based upon the spectrophotometric standard stars that are included in the observation set of each plate. These calibration are what we use as a "pseudo-truth" for comparisons of our network results.

## 5. Experiments and Results

We train and evaluate multiple networks based on various combinations of the below (hyper-)parameters:

- Latent-space dimensionality
- Velocity randomization level

For our main experiments, that include hyper-parameter sweeping and controlled tests, we mainly use the HARPS dataset. Other datasets are used for comparative testing of the method in extreme conditions.

<sup>4</sup> <https://data.sdss.org/sas/dr17/>

<sup>5</sup> <https://data.sdss.org/datamodel/>

### 5.1. Main Results

Figure 5 illustrates a few examples of how the method manages to reject the telluric lines and preserve the stellar features. The example spectra and regions are specifically chosen to rule out potential naive hypotheses for how the network rejects telluric lines. In other words, the results confirm that the network has learned a semantic representation of the constituent components and is separating the sources in that feature space, as opposed to e.g. simply having "missed" narrower lines (simple averaging, low-pass filtering). In the caption of fig. 5 a few other such hypotheses are elaborated and rejected.

### 5.2. Quantitative Evaluation

Various (hyper-)parameters, such as the degree of compression during dimensionality reduction, or the resolution of the input data, may influence the capability of the network in rejecting the telluric lines. Precisely, there is always a trade off between telluric-rejection and stellar-reconstruction. Therefore, we develop and incorporate the below mutual metrics to quantify both aspects at the same time:

$$Q^t = \frac{\sum (M^t | \hat{S} - \tilde{G})}{\sum M^t} \quad (9)$$

where  $Q^t$  is a proxy for the quality of rejection of telluric lines.  $\hat{S}$  represents the reconstructed spectrum (i.e. the direct output of the network) and  $\tilde{G}$  is the *pseudo ground truth*.  $\tilde{G}$  is a *corrected* version of the output of molecfit in case of HARPS data, and a modified version of the publicly available calibrated spectra in case of SDSS.  $M^t$  is a binary mask; a vector of the same size of the input, having ones at all pixels containing *known* telluric lines, and zeros everywhere else. Note that the subscript  $i$ , indexing each observed spectrum, is omitted in  $Q^t$ ,  $\hat{S}$ ,  $\tilde{G}$  and  $M^t$  for the sake of simplicity, and the summation is calculated over all the pixels of each spectrum.

We similarly define the dual metric for measuring the reconstruction (preservation) of the stellar features as follows:

$$Q^s = \frac{\sum (M^s | 1 - \frac{\hat{S}}{\tilde{G}})}{\sum M^s} \quad (10)$$

where  $Q^s$  is, conversely, a proxy for the quality of stellar reconstruction. Note that both of the above are metrics of a distance nature, and hence, the lower the better.

### 5.3. The Effect of Compression

It is reasonable to expect, and is supported by our experiments that, with a lower dimensionality at the information bottleneck of the network, the network's capacity for preserving many concurrent features during compression diminishes. This results in a higher rejection of *details* in the reconstructed spectra, which can be naively interpreted as an improvement in telluric line rejection – a decrease in  $Q^t$ . Note however that stellar reconstruction quality can get worse at the same time, and so the two metrics need to be considered at the same time.

Table 1 compares results of various runs with different dimensionalities at the latent space on a fixed subset of HARPS spectra. Note how the stellar reconstruction quality starts to decay by increasing the compression (lower latent dimensions). On

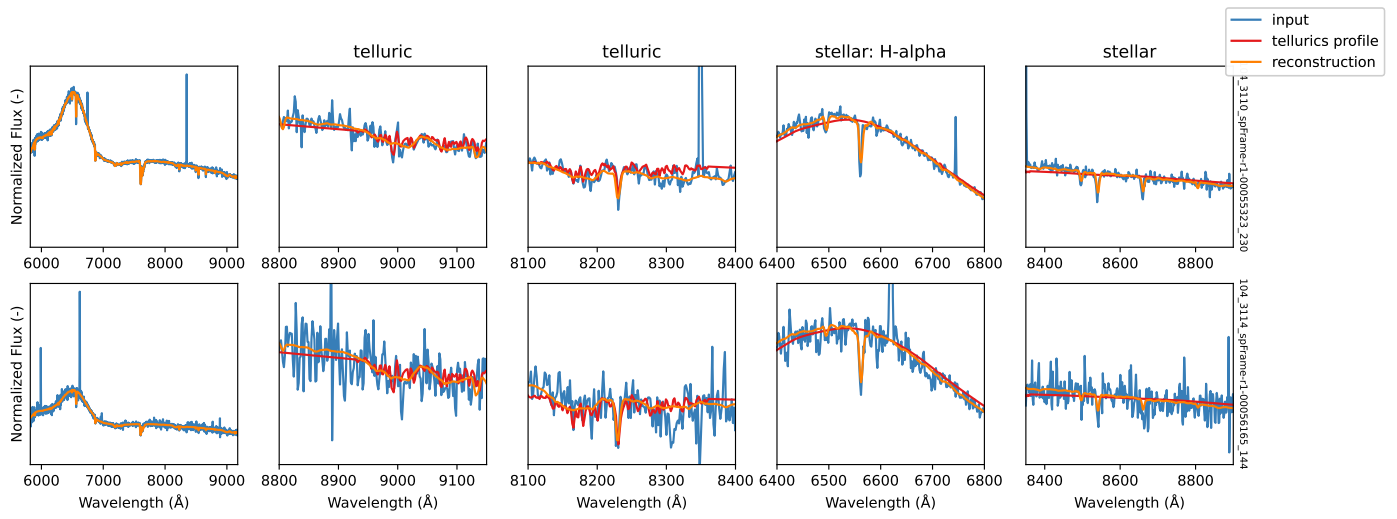


**Fig. 6.** Test results on a low-resolution data collection: SDSS. On the left, the whole spectrum is depicted, while the other columns depict various regions of interest along the wavelength axis, so the qualitative performance of the method can be assessed on specific stellar and telluric features. Note that since pseudo-truth data is not easily obtainable in this case, we over-plot a "tellurics profile" in red, just for visual comparison. It should be interpreted differently from the pseudo-truth curves in other figures, as it does follow the telluric lines. Stellar features are preserved very well, even in bad signal-to-noise conditions. Some of the wider telluric lines, however, are not fully rejected in this case due to the significantly low resolution as compared to HARPS. Please refer to the main text for a more detailed discussion.

Latent Dim.↓	Telluric	Stellar
8	0.053	0.015
32	0.055	0.012
128	0.063	0.014
1024	0.176	0.012

**Table 1.** Quality of stellar line reconstruction vs. telluric line rejection on HARPS, for different configurations of the network. Latent Dim. is the number of dimensions of the *code*, or the latent representation. A lower number is better in both columns.

the other hand, by increasing the number of latent nodes, the network starts to become too powerful, managing to reconstruct both components and losing the source separation capability.

#### 5.4. The Effect of Velocity-Whitening

To demonstrate the effect of the whitening step, we compare the results of two experiments in controlled conditions. The first experiment is run on HARPS spectra in topocentric frame, where telluric lines are all aligned – zero velocity randomization. Then we apply velocity whitening, sampling  $v_i$  from the uniform distribution:  $V \sim U(-30\text{km/s}, 30\text{km/s})$ . All other configurations of the test are kept fixed. Table 2 shows a clear difference in the telluric rejection performance of the two runs.

HARPS		
	Telluric	Stellar
Topocentric	0.199	0.018
Rand. Velocity	0.063	0.014

**Table 2.** Comparison of two experiments with zero velocity randomization ('Topocentric') and  $V \sim U(-30\text{km/s}, 30\text{km/s})$  ('Rand. Velocity').

#### 5.5. HARPS vs. SDSS: High- vs. Low-Resolution

Figure 6 depicts the results of applying our method on SDSS spectra. The extremely low pixel resolution we used for this dataset (1.66Å as opposed to 0.01Å for HARPS), makes this in practice a stress test for our method, since many of the telluric lines get merged, appearing as wide artifacts. However, the method performs at an acceptable level. E.g. the middle column of fig. 6 shows how the method misses the very wide telluric artifact while managing to reject the neighboring telluric lines. In general, it seems our method can "hunt" telluric lines up until the point the resolution goes so low that merging/blending of the lines converts them to "slow" artifacts.

## 6. Conclusions and Future Directions

We presented a method that, by incorporating a Big Data-inspired view at stellar spectra, exploits the statistical independence of the radial velocity of stars with telluric lines in their observed spectra, reinforces it using a novel trick, and utilizes a fully unsupervised convolutional neural network to reject the undesirable part.

The method is superior to existing, traditional telluric line removal tools in terms of preparation effort, performance, and accuracy. The fact that it is fully unsupervised, obviates the need for any kind of model parameter tuning – which is the case in e.g. molecfit, where a list of wavelengths should be manually specified to initialize the model. Training the model, in practice, calls for merely passing a large number of spectra through the network – and it will do the rest.

Training one network suffices for one whole data collection. Once trained, it processes each spectrum in a fraction of a second – depending on the size of the spectrum and, consequently, the size of the network. But the speed-up does not sacrifice accuracy; as seen in section 5, it can even detect and suppress hard-to-locate lines which are missed by molecfit – the opposite may happen too, though in rarer situations.

Nevertheless, the current version is still a demonstration of a research product, showcasing the strengths of a fully unsupervised approach. But for Stellar Karaoke to become a ready-to-use package in every application, more work is required. Notably, the decision of which component to keep and which one to reject (stellar vs. telluric), should not be left to the network. It can be enforced by a minimal supervision.

*Acknowledgements.* Some of the experiments demonstrated in this work have been run on compute servers provided by ESO, during NS's collaboration with the ESCAPE project between 2019 and 2021.

## References

Abazajian, K. N., Adelman-McCarthy, J. K., Agüeros, M. A., et al. 2009, *ApJS*, 182, 543

Abdurro'uf, Accetta, K., Aerts, C., et al. 2022, *ApJS*, 259, 35

Allart, R., Lovis, C., Faria, J., et al. 2022, *A&A*, 666, A196

Artigau, É., Astudillo-Defru, N., Delfosse, X., et al. 2014, in *Observatory Operations: Strategies, Processes, and Systems V*, Vol. 9149, International Society for Optics and Photonics, 914905

Bailer-Jones, C. A., Irwin, M., & Von Hippel, T. 1998, *Monthly Notices of the Royal Astronomical Society*, 298, 361

Connolly, A. J., Szalay, A. S., Bershadsky, M. A., Kinney, A. L., & Calzetti, D. 1995, *AJ*, 110, 1071

Eldar, Y. C. & Oppenheim, A. V. 2003, *IEEE Transactions on Information Theory*, 49, 1846

Gullikson, K., Dodson-Robinson, S., & Kraus, A. 2014, *AJ*, 148, 53

Gunn, J. E., Siegmund, W. A., Mannery, E. J., et al. 2006, *AJ*, 131, 2332

Hadrava, P. 1997, *Astronomy and Astrophysics Supplement Series*, 122, 581

Hinton, G. E. & Salakhutdinov, R. R. 2006, *Science*, 313, 504

Hrudková, M. & Harmanec, P. 2005, *A&A*, 437, 765

Jolliffe, I. T. & Cadima, J. 2016, *Philosophical Transactions of the Royal Society A: Mathematical, Physical and Engineering Sciences*, 374, 20150202

Kessy, A., Lewin, A., & Strimmer, K. 2018, *The American Statistician*, 72, 309

Kingma, D. P. & Welling, M. 2014, arXiv:1312.6114 [cs, stat], arXiv: 1312.6114

Li, G. & Zhang, J. 1998, *Sankhyā: The Indian Journal of Statistics, Series A*, 119

Mayor, M., Pepe, F., Queloz, D., et al. 2003, *The Messenger*, 114, 20

Portillo, S. K. N., Parejko, J. K., Vergara, J. R., & Connolly, A. J. 2020, *AJ*, 160, 45

Rockosi, C. M., Lee, Y. S., Morrison, H. L., et al. 2022, *ApJS*, 259, 60

Sedaghat, N., Romaniello, M., Carrick, J. E., & Pineau, F.-X. 2021, *Monthly Notices of the Royal Astronomical Society*, 501, 6026

Smeek, S. A., Gunn, J. E., Uomoto, A., et al. 2013, *AJ*, 146, 32

Smette, A., Sana, H., Noll, S., et al. 2015, *A&A*, 576, A77

Stoughton, C., Lupton, R. H., Bernardi, M., et al. 2002, *AJ*, 123, 485

Ulmer-Moll, S., Figueira, P., Neal, J. J., Santos, N. C., & Bonnefoy, M. 2019, *A&A*, 621, A79

Vacca, W. D., Cushing, M. C., & Rayner, J. T. 2003, *PASP*, 115, 389

Wang, K., Guo, P., & Luo, A.-L. 2016a, *Monthly Notices of the Royal Astronomical Society*, 465, 4311

Wang, Y., Yao, H., & Zhao, S. 2016b, *Neurocomputing*, 184, 232

Yang, T. & Li, X. 2015, *Monthly Notices of the Royal Astronomical Society*, 452, 158

Yanny, B., Rockosi, C., Newberg, H. J., et al. 2009, *AJ*, 137, 4377

Zhang, C., Wang, J., Zhao, N., & Zhang, D. 2004, *Pattern Recognition*, 37, 325

## Appendix A: Wavelength Transformation and Convolution

$$\begin{aligned} x(\lambda) &= z(\lambda) * h(\lambda) \\ &= \int_w z(w)h(\lambda - w)dw \end{aligned} \quad (\text{A.1})$$

$$\begin{aligned} x(\lambda'_i) &= x(a\lambda) \\ &= \int_w z(w)h(a\lambda - w)dw \end{aligned} \quad (\text{A.2})$$

$$\text{Let } w = au, \quad (\text{A.3})$$

$$x(\lambda'_i) = a \int_u z(au)h(a\lambda - au)du \quad (\text{A.4})$$

$$\text{Let } z(au) = z'(u), \quad h(au) = h'(u) \quad (\text{A.5})$$

$$\begin{aligned} \implies x(\lambda'_i) &= a \int_u z'(u)h'(\lambda - u)du \\ &= a z'(\lambda) * h'(\lambda) \\ &= a z(a\lambda) * h(a\lambda) \\ &= a z(\lambda'_i) * h(\lambda'_i) \end{aligned} \quad (\text{A.6})$$

The same could be shown in a rather shorter way using the Fourier transform. However, to avoid confusion between the terms *frequency* and *wavelength* used in two different domains, here we use the direct expansion of the convolution operator.